

Observation of Time-Crystalline Eigenstate Order on a Quantum Processor

Google Quantum AI and collaborators^{†,*}

Quantum many-body systems display rich phase structure in their low-temperature equilibrium states¹. However, much of nature is not in thermal equilibrium. Remarkably, it was recently predicted that out-of-equilibrium systems can exhibit novel dynamical phases^{2–8} that may otherwise be forbidden by equilibrium thermodynamics, a paradigmatic example being the discrete time crystal (DTC)^{7,9–14}. Concretely, dynamical phases can be defined in periodically driven many-body localized systems via the concept of eigenstate order^{7,15,16}. In eigenstate-ordered phases, the *entire* many-body spectrum exhibits quantum correlations and long-range order, with characteristic signatures in late-time dynamics from *all* initial states. It is, however, challenging to experimentally distinguish such stable phases from transient phenomena, wherein few select states can mask typical behavior. Here we implement a continuous family of tunable CPHASE gates on an array of superconducting qubits to experimentally observe an eigenstate-ordered DTC. We demonstrate the characteristic spatiotemporal response of a DTC for generic initial states^{7,9,10}. Our work employs a time-reversal protocol that discriminates external decoherence from intrinsic thermalization, and leverages quantum typicality to circumvent the exponential cost of densely sampling the eigenspectrum. In addition, we locate the phase transition out of the DTC with an experimental finite-size analysis. These results establish a scalable approach to study non-equilibrium phases of matter on current quantum processors.

In an equilibrium setting, quantum phases of matter are classified by long-range order or broken symmetries in low-temperature states (Fig. 1a). The existence of ordered phases in periodically driven (Floquet) systems, on the other hand, is counterintuitive: Since energy is not conserved, one expects thermalization to a featureless maximum-entropy state that is incompatible with quantum order. However, this heat death is averted in the presence of many-body localization (MBL), where strong disorder causes the emergence of an extensive number of local conservation laws which prevent thermalization^{17–22}, making it possible to stabilize intrinsically dynamical phases⁷.

Dynamics in a Floquet system is governed by a unitary time evolution operator, whose eigenvalues lie on the unit

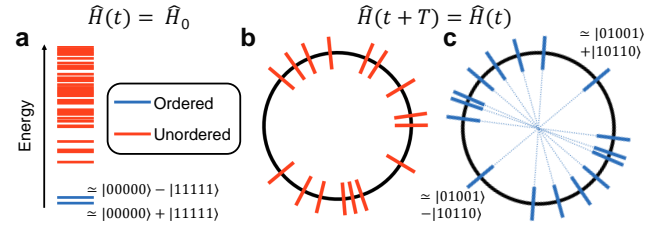


FIG. 1. **Order in eigenstates.** a, Equilibrium phases are characterized by long-range order in low-energy eigenstates of time-independent Hamiltonians, e.g. an Ising ferromagnet with a pair of degenerate ground states that resemble “Schrödinger cats” of polarized states. b, Floquet systems typically have no ordered states in the spectrum. c, In MBL Floquet systems, every eigenstate can show order. In MBL-DTC, every eigenstate resembles a long-range ordered “Schrödinger cat” of a random configuration of spins and its inversion, with even/odd superpositions split by π .

circle. While the entire Floquet spectrum is featureless in a thermalizing phase (Fig. 1b), an MBL Floquet phase can have an order parameter associated with each eigenstate. As an example, in the spatiotemporally-ordered MBL-DTC, the spectrum has a distinctive pattern of pairing between “Schrödinger cat” states that are separated by an angle π (Fig. 1c)^{7,9,10}. This pairing manifests as a stable sub-harmonic response, wherein local observables show period-doubled oscillations that spontaneously break the discrete time translation symmetry of the drive for infinitely long times. The unique combination of spatial long-range order and time translation symmetry breaking in an isolated dissipation-free quantum many-body system is the hallmark of the MBL-DTC.

Experimentally observing a non-equilibrium phase such as the MBL-DTC is a challenge due to limited programmability, coherence and size of Noisy Intermediate Scale Quantum (NISQ) hardware. Sub-harmonic response, by itself, is not a unique attribute of the MBL-DTC; rather, it is a feature of many dynamical phenomena whose study has a rich history^{23,24} (See also Ch. 8 in Ref.¹²). Most recently, interesting DTC-like dynamical signatures have been observed in a range of quantum platforms^{25–28}. Such signatures, however, are transient, arising from slow or prethermal dynamics from special initial states^{12,29–32}, and are separated from the MBL-DTC by a spectral phase transition where eigenstate order disappears. Thus, despite the recent progress, observing an MBL-DTC remains an outstanding challenge^{12,32}.

Here we perform the following necessary benchmarks for experimentally establishing an eigenstate-ordered non-equilibrium phase of matter: (i) Drive parameters

^{*} Corresponding authors: V. Khemani: vkhemani@stanford.edu; P. Roushan: pedramr@google.com

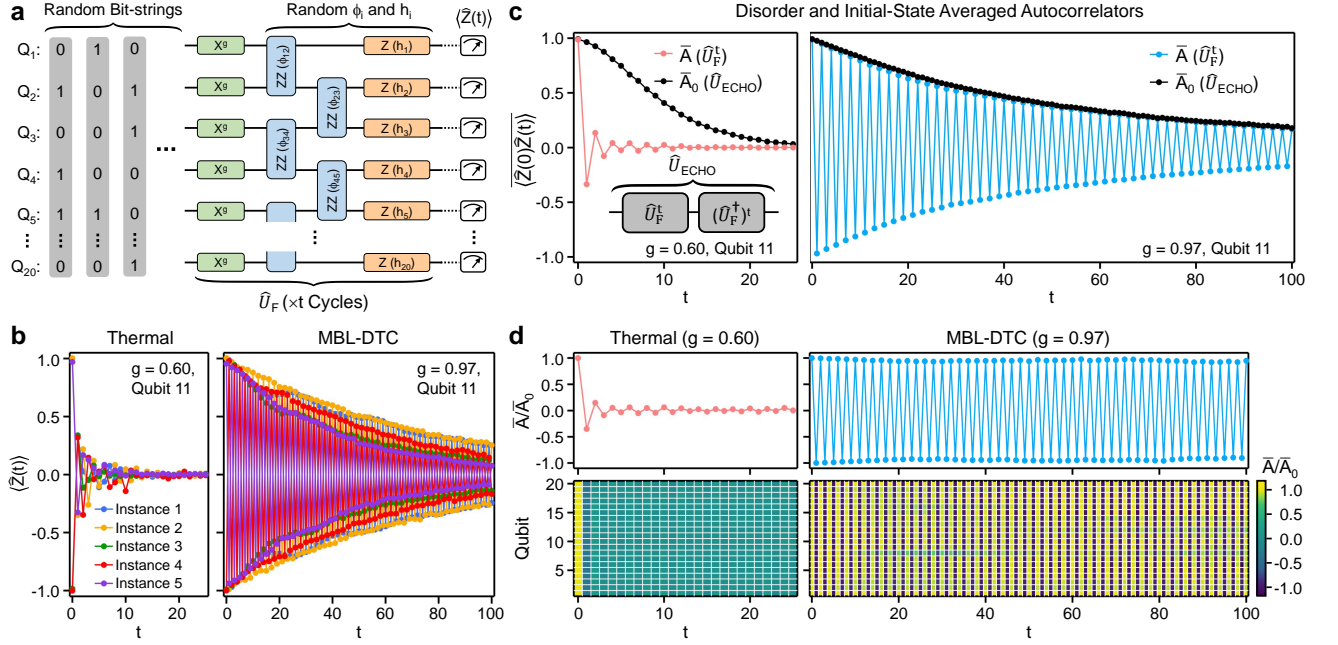


FIG. 2. **Observing a many-body localized discrete time-crystal.** **a**, Schematic of the experimental circuit composed of t identical cycles of the unitary \hat{U}_F . The local polarization of each qubit, $\langle \hat{Z}(t) \rangle$, is measured at the end. In the following panels, we investigate a number of disorder instances each with a different random bit-string initial state. **b**, Experimental values of $\langle \hat{Z}(t) \rangle$ measured at qubit 11. Data are shown for five representative circuit instances deep in the thermal ($g = 0.60$) and MBL-DTC ($g = 0.97$) phases. **c**, Autocorrelator $\bar{A} = \langle \hat{Z}(0)\hat{Z}(t) \rangle$ at qubit 11, obtained from averaging the results of 36 circuit instances. For the same circuit instances, the average autocorrelator at the output of $\hat{U}_{\text{ECHO}} = (\hat{U}_F^\dagger)^t \hat{U}_F^t$ is also measured and its square root, \bar{A}_0 , is shown alongside \bar{A} for comparison. **d**, Top panels: The ratio \bar{A}/\bar{A}_0 obtained from panel **c**. Bottom panels: \bar{A}/\bar{A}_0 as a function of t and qubit location.

are varied in order to demonstrate stability of the phase in an extended parameter region and across disorder realizations; The limitations of (ii) finite size and (iii) finite coherence time are addressed, respectively, by varying the number of qubits in the system and by separating effects of extrinsic decoherence from intrinsic thermalization; (iv) The existence of eigenstate order across the *entire* spectrum is established. The flexibility of our quantum processor, combined with the scalable experimental protocols devised in the following, allows us to fulfill these criteria and observe time-crystalline eigenstate order.

The experiment is conducted on an open-ended, linear chain of $L = 20$ superconducting transmon qubits (Q_1 through Q_{20}) that are isolated from a two-dimensional grid. We drive the qubits via a time-periodic (Floquet) circuit \hat{U}_F^t with t identical cycles (Fig. 2a) of \hat{U}_F :

$$\hat{U}_F = \underbrace{e^{-\frac{i}{2} \sum_i h_i \hat{Z}_i}}_{\text{longitudinal fields}} \underbrace{e^{-\frac{i}{4} \sum_i \phi_i \hat{Z}_i \hat{Z}_{i+1}}}_{\text{Ising interaction}} \underbrace{e^{-\frac{i}{2} \pi g \sum_i \hat{X}_i}}_{x \text{ rotation by } \pi g} \quad (1)$$

where \hat{X}_i and \hat{Z}_i are Pauli operators. Each ϕ_i (h_i) is sampled randomly from $[-1.5\pi, -0.5\pi]$ ($[-\pi, \pi]$) for every realization of the circuit. Overall, \hat{U}_F implements an interacting Ising model that is periodically “kicked” by a transverse pulse that rotates all qubits by πg about the x axis. In this work, g is tuned within the range $[0.5, 1.0]$ to

explore the DTC phase and its transition into a thermal phase. At $g = 1$, the model implements a π pulse which exactly flips all qubits (in the z basis) and returns them to the initial state over two periods. A key signature of the DTC is the presence of *robust* period doubling, *i.e.* extending over a finite extent in parameter space, even as g is tuned away from 1. Strong Ising interactions, which produce long-range *spatial* order, are essential for this robustness^{7,10}. This is in contrast to a system of decoupled qubits ($\phi = 0$) which rotate by a continuously varying angle πg every period instead of being locked at period doubling. Prior theoretical work³² has shown that model (1) is expected to be in an MBL DTC phase in the range $g > g_c$, and transition to a thermal phase at a critical value $g_c \approx 0.84$.

Achieving MBL in this model for $g \sim 1$ requires disorder in the two-qubit interaction, ϕ_i , which is even under Ising symmetry^{12,32}, $\prod_i \hat{X}_i$, a condition that was not met by some past DTC experiments^{26,27}. Ising-odd terms, *i.e.* h_i , are approximately dynamically decoupled by the x pulses over two periods, thereby lowering their effective disorder strength and hindering localization (in the absence of independent disorder in the ϕ_i). Utilizing newly developed CPHASE gates (see SM for details) with continuously tunable conditional phases allows us to engineer strong disorder in ϕ_i to fulfill this key requirement.

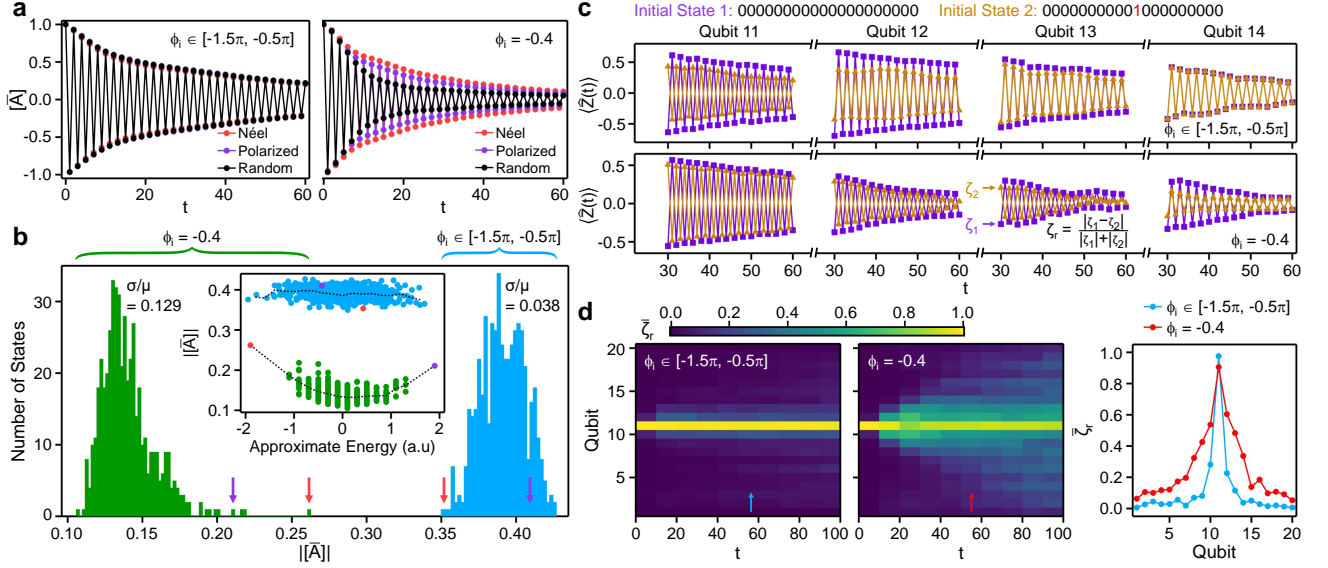


FIG. 3. **Observing eigenstate order and distinguishing it from transient phenomena.** **a**, Site- and disorder-averaged autocorrelators $[A]$ measured with $g = 0.94$. In the left panel (MBL-DTC), each data set is averaged over 24 disorder instances of ϕ_i and h_i , with the initial state fixed at one of the following: Néel: $|01\rangle^{\otimes 10}$, Polarized: $|0\rangle^{\otimes 20}$, Random: $|00111000010011001111\rangle$. In the right panel (thermalizing), the same values of h_i and initial states are used but $\phi_i = -0.4$. **b**, Histograms of $[|A|]$, from 500 random bit-string initial states, averaged over cycles 30 and 31 and the same disorder instances as in panel **a**. σ/μ , where σ (μ) is the standard deviation (mean) of $[|A|]$, is also listed. Location of the polarized (Néel) state is indicated by a purple (red) arrow. Inset: same collection of $[|A|]$ plotted over the energies of the bit-string states, calculated from the effective Hamiltonian \hat{H}_{eff} approximating the drive (see text). Dashed lines show averaged values within energy windows separated by 0.2. **c**, $\langle \hat{Z}(t) \rangle$ for two bit-string initial states that differ only at Q_{11} . Top panel shows a single circuit instance with disordered ϕ_i and bottom panel shows an instance with uniform $\phi_i = -0.4$. **d**, Left and middle panels: Relative difference between the two signals \bar{z}_r as a function of t and qubit location, averaged over time windows of 10 cycles and over 64 disorder instances for \hat{U}_F and 81 instances for \hat{U}'_F . Right panel: Qubit dependence of \bar{z}_r , averaged from $t = 51$ to $t = 60$.

We first measure the hallmark of an MBL-DTC: the persistent oscillation of local qubit polarizations $\langle \hat{Z}(t) \rangle$ at a period twice that of \hat{U}_F , irrespective of the initial state^{7,9,12,32}. This subharmonic response is probed using a collection of random bit-string states, e.g. $|01011\dots\rangle$ where 0(1) denotes a single-qubit ground(excited) state in the z basis. For each bit-string state, we generate a random instance of \hat{U}_F , and then measure $\langle \hat{Z}(t) \rangle$ every cycle. Figure 2b shows $\langle \hat{Z}(t) \rangle$ in a few different instances for a qubit near the center of the chain, Q_{11} , measured with $g = 0.60$ and $g = 0.97$. The former is deep in the thermal phase and indeed we observe rapid decay of $\langle \hat{Z}(t) \rangle$ toward 0 within 10 cycles for each instance. In contrast, for $g = 0.97$, $\langle \hat{Z}(t) \rangle$ shows large period-doubled oscillations persisting to over 100 cycles, suggestive of an MBL-DTC phase. The disorder averaged autocorrelator, $\bar{A} = \langle \hat{Z}(0)\hat{Z}(t) \rangle$, shows similar features (Fig. 2c).

We note that the data for $g = 0.97$ is modulated by a gradually decaying envelope, which may arise from either external decoherence or slow internal thermalization^{25,30}. To establish DTC, additional measurements are needed to distinguish between these two mechanisms. This is achieved via an “echo” circuit $\hat{U}_{\text{ECHO}} = (\hat{U}_F^\dagger)^t \hat{U}_F^t$ which reverses the time evolution after t steps. Deviations of

\hat{U}_{ECHO} from the identity operation are purely due to decoherence, and can be quantified via decay of the autocorrelator $A_0 \equiv (\langle \hat{Z} \hat{U}_{\text{ECHO}}^\dagger \hat{Z} \hat{U}_{\text{ECHO}} \rangle)^{1/2}$ (the square root accounts for the fact that \hat{U}_{ECHO} acts twice as long as \hat{U}_F). A similar time-reversal technique was recently used in the study of out-of-time-ordered commutators in thermalizing random circuits³³.

Comparison between the disorder averaged \bar{A}_0 and \bar{A} reveals qualitatively different behaviors in the two phases (Fig. 2c). In the thermal phase $g = 0.60$, \bar{A} approaches 0 much more quickly than \bar{A}_0 does, indicating that the observed decay of \bar{A} is mostly induced by intrinsic thermalization. In the MBL-DTC phase $g = 0.97$, \bar{A}_0 nearly coincides with the envelope of \bar{A} , suggesting that decay of the latter is primarily induced by decoherence. The reference signal \bar{A}_0 may be used to normalize \bar{A} and reveal its ideal behavior: \bar{A}/\bar{A}_0 , shown in the upper panels of Fig. 2d, decays rapidly for $g = 0.60$ but retains near-maximal amplitudes for $g = 0.97$. Similar contrast between the two phases is seen in the error-mitigated autocorrelators \bar{A}/\bar{A}_0 for all qubits (bottom panel of Fig. 2d). The observation of a stable noise-corrected sub-harmonic response is suggestive of an MBL-DTC phase.

We now turn to a systematic analysis of the next requirement necessary to establish an MBL-DTC: namely

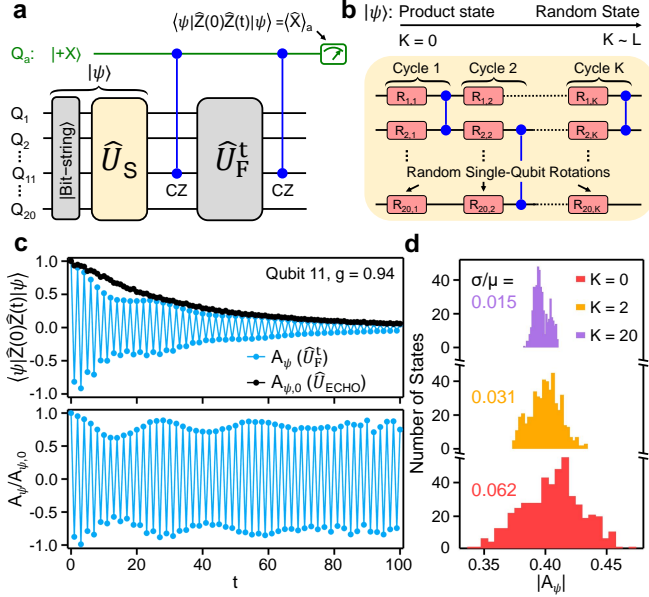


FIG. 4. Probing average spectral response via quantum typicality. **a**, Schematic for measuring the autocorrelator, $A_\psi = \langle \psi | \hat{Z}(0) \hat{Z}(t) | \psi \rangle$, on Q_{11} , of a scrambled quantum state $|\psi\rangle$. $|\psi\rangle$ is created by passing a bit-string state through a scrambling circuit, \hat{U}_S . An ancilla qubit Q_a prepared in $|+X\rangle$ interacts with one of the qubits (Q_{11}) via a CZ gate before and after \hat{U}_F^t . The x -axis projection of Q_a , $\langle \hat{X} \rangle_a$, is measured at the end. **b**, \hat{U}_S contains K layers of CZ gates interleaved with random single-qubit rotations, $R_{i,k}$, around a random axis along the equatorial plane of the Bloch sphere by an angle $\in [0.4\pi, 0.6\pi]$. **c**, Upper panel: A_ψ for a single disorder instance with $K = 20$ cycles in \hat{U}_S . The square-root of the autocorrelator obtained by replacing \hat{U}_F^t with \hat{U}_{ECHO} , $A_{\psi,0}$, is also shown. Bottom panel: Normalized autocorrelator, $A_\psi/A_{\psi,0}$, as a function of t . **d**, Histograms of $|A_\psi|$ from a single disorder instance, averaged over cycles 30 and 31. Each histogram corresponds to a different number of scrambling cycles, K , and includes data from 500 random initial bit-string states fed through the scrambling circuit.

the presence of eigenstate order across the entire spectrum which, in turn, implies that sub-harmonic response should not be strongly affected by the choice of initial states. In contrast, various prethermal mechanisms in driven systems predict strong dependence of the thermalization rate on the initial state, e.g. through its quantum numbers^{27,31} or its energy under an effective time-independent Hamiltonian \hat{H}_{eff} ^{29,34,35} that approximately governs the dynamics for small system sizes and/or finite times. To elucidate this aspect of the MBL-DTC phase, we analyze in detail the distribution of autocorrelator values over initial bit-string states.

We begin by examining the position- and disorder-averaged autocorrelator $[\bar{A}]$ over three representative bit-string initial states, shown in the left panel of Fig. 3a. The square brackets indicate averaging over qubits in the chain (excluding the edge qubits Q_1, Q_{20} , which may be

affected by the presence of edge modes independent of the bulk DTC response³⁶). The three time traces are nearly indistinguishable. This behavior is in clear contrast with a model without eigenstate order, implemented by a family of drives \hat{U}'_F where the ϕ_i angles are set to a uniform value³⁷, $\phi_i = -0.4$. Without disorder in the ϕ_i , the drive \hat{U}'_F is not asymptotically localized but exhibits transient DTC-like behavior. Here, $[\bar{A}]$ for \hat{U}'_F (disorder averaged over random h_i only), shown in the right panel of Fig. 3a, reveals markedly different decay rates for the three states. The random bit-string state, in particular, decays faster than the polarized or Néel states.

A more comprehensive analysis, presented in Fig. 3b, is based on sampling the absolute values of $[\bar{A}]$ for 500 random initial bit-string states (averaged over cycles 30 and 31). For the MBL-DTC \hat{U}_F , the histogram is tight, with a relative standard deviation (ratio of standard deviation to mean, σ/μ) of 0.038. Here the non-zero value of σ likely stems from finite experimental accuracy and number of disorder instances, as analysis in the SM shows that $[\bar{A}]$ is independent of the initial state. In contrast, the \hat{U}'_F model shows a broader distribution with a much lower mean, and with $\sigma/\mu = 0.129$. Moreover, the histogram is asymmetrical, with outliers at high $[\bar{A}]$ including the polarized and Néel states (51% and 88% higher than the mean, respectively). These two states are special because they are low temperature states that sit near the edge of the spectrum of \hat{H}_{eff} (see SM). Plotting the autocorrelator $[\bar{A}]$ against the energy of each bitstring under \hat{H}_{eff} , in the inset of Fig. 3b, reveals a clear correlation. No such correlation is present in the MBL model.

Independent confirmation of MBL as the mechanism underlying the stability of DTC is achieved by characterizing the propagation of correlations. In MBL dynamics, local perturbations spread only logarithmically in time¹⁹, as opposed to algebraic ($\sim t^\alpha$) spreading in thermalizing dynamics. We prepare two initial bitstring states differing by only a single bit-flip at Q_{11} and measure $\langle \hat{Z}(t) \rangle$ for each site in both states (Fig. 3c). It can be seen that the difference in the two signals, ζ_1 and ζ_2 , decays rapidly with the distance from Q_{11} for disordered ϕ_i and becomes undetectable at Q_{14} . On the other hand, for uniform $\phi_i = -0.4$, ζ_1 and ζ_2 have a much more pronounced difference which remains significant at Q_{14} . This difference is further elucidated by the ratio $\zeta_r = |\zeta_1 - \zeta_2| / (|\zeta_1| + |\zeta_2|)$, shown in Fig. 3d. Physically, ζ_r corresponds to the relative change in local polarization as a result of the bit flip, and is inherently robust against qubit decoherence (see SM). We observe that up to $t = 100$, ζ_r remains sharply peaked around the initial perturbation (Q_{11}) for disordered ϕ_i . In contrast, a propagating light cone is visible for $\phi_i = -0.4$, with the perturbation reaching all qubits across the chain as t increases. The spatial profiles of ζ_r at $t = 51$ to $t = 60$ (right panel of Fig. 3d) show that ζ_r is much sharper for disordered ϕ_i . This slow propagation provides strong indication of MBL and another experimental means of distinguishing eigenstate-ordered phases from transient phenomena.

Our measurement of $\langle \bar{A} \rangle$ for 500 initial states in Fig. 3d provides clear evidence of initial state independence. Still, a direct sampling of states is practically limited to small fractions of the computational basis (0.05% in this case) and would suffer from the exponential growth of the Hilbert space on larger systems. A more scalable alternative is to use random, highly entangled states to directly measure spectrally-averaged quantities (quantum typicality^{38–40}). The autocorrelator A averaged over all 2^L bitstrings agrees, up to an error exponentially small in L , with $A_\psi = \langle \psi | \hat{Z}(0) \hat{Z}(t) | \psi \rangle$, where $|\psi\rangle$ is a typical Haar-random many-body state in the Hilbert space of L qubits. We prepare such a state by evolving a bitstring with a random circuit \hat{U}_S of variable depth K (Fig. 4b), and couple an ancilla qubit to the system to measure the two-time operator $\hat{Z}(0) \hat{Z}(t)$ (Fig. 4a). Experimental results for the error-mitigated, spectrally averaged signal $A_\psi/A_{\psi,0}$ on qubit Q_{11} (Fig. 4c) show behavior consistent with a stable MBL-DTC. The effect of the state-preparation circuit \hat{U}_S is illustrated by the dependence of the relative standard deviation σ/μ for A_ψ on K . As shown in Fig. 4d, σ/μ steadily decreases as K increases, reducing from a value of 0.062 at $K = 0$ to a value of 0.015 at $K = 20$. This is consistent with the fact that $|\psi\rangle$ becomes closer to a Haar-random state as K increases. We use a single disorder instance to study the convergence of the quantum typicality protocol because disorder averaging independently leads to narrow distributions even for $K = 0$ (Fig. 3b).

The scaling with L of the spectrally-averaged autocorrelator, at a time $t \sim \text{poly}(L)$, provides a sharp diagnostic: this saturates to a finite value in the MBL-DTC, while it scales to zero with increasing L in transient cases (where, for instance, a vanishing fraction of the spectrum of an appropriate \hat{H}_{eff} shows order). While the averaged autocorrelator may be unduly affected by outlier states and/or long (but $O(1)$) thermalization times at small system sizes and times (thereby making the complementary bitstring analysis of Fig. 3 essential), the polynomial scaling of this protocol establishes a proof of principle for efficiently verifying the presence or absence of an MBL DTC in a range of models as quantum processors scale up in size to surpass the limits of classical simulation⁴¹.

Finally, we systematically vary g in small increments and obtain an experimental finite-size analysis to establish the extent of the MBL phase and the transition out of it. Sharply defining phases of matter, whether in or out of equilibrium, requires a limit of large system size. Thus it is important to examine the stability of the MBL-DTC and thermalizing regimes observed in our finite-size quantum processor as the size of the system is increased. To address this, we measure an Edwards-Anderson spin glass order parameter^{42,43},

$$\chi^{\text{SG}} = \frac{1}{L-2} \sum'_{i \neq j} \langle \hat{Z}_i \hat{Z}_j \rangle^2 \quad (2)$$

(the primed sum excludes edge qubits Q_1, Q_L), as a function of time. This quantity measures the persistence of

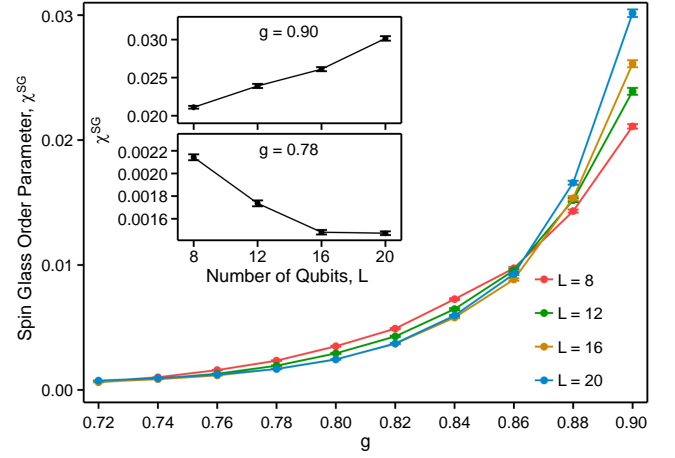


FIG. 5. **Estimating phase-transition by varying system size.** Spin-glass order parameter χ^{SG} as a function of g for different chain lengths L , measured between $t = 51$ and $t = 60$. Every data point is averaged over 40 disorder instances. To construct χ^{SG} , we sample 40000 bit-strings at the output of \hat{U}_F^t for each cycle and disorder instance. To address the inhomogeneity of qubit coherence, smaller qubit chains are also averaged over different possible combinations of qubits. For example, $L = 12$ is averaged over 12-qubit chains made from Q_1 through Q_{12} , Q_3 through Q_{15} etc. Error bars correspond to statistical errors (estimated by resampling data from the 40 disorder instances via the jackknife method). Contribution of hardware (e.g. gate) errors to χ^{SG} is not included in the error bars. Inset shows the size-dependence of χ^{SG} for two different values of g .

random (“glassy”) spatial patterns in the initial bitstring state: at late times, it vanishes with increasing L in the thermalizing phase $g < g_c$, while it is extensive in the MBL-DTC $g > g_c$. As a result, it is expected to show a finite-size crossing at $g \simeq g_c$ (though the precise location is subject to strong finite-size and finite-time drifts^{44,45}). Experimentally, χ^{SG} is constructed from bit-string samples obtained by jointly reading out all qubits and then averaged over cycles and disorder instances (Fig. 5). The size of the qubit chain is varied by restricting the drive \hat{U}_F to contiguous subsets of 8, 12, and 16 qubits (as well as the entire 20-qubit chain). We observe increasing (decreasing) trends in χ^{SG} vs L when g is above (below) a critical value g_c . The data indicate $0.83 \lesssim g_c \lesssim 0.88$, consistent with numerical simulations (see SM).

In conclusion, we have demonstrated the possibility of engineering and characterizing non-equilibrium phases of matter on a quantum processor, providing direct experimental observation of an eigenstate-ordered MBL-DTC. The scalability of our protocols sets a blueprint for future studies of non-equilibrium phases and phase transitions on complex quantum systems beyond classical simulability. The efficient verification of eigenstate order can inspire a general strategy for establishing whether a desired property, such as a particular phase, is in fact present in a quantum processor.

[†] Google Quantum AI and Collaborators

Xiao Mi^{1,*}, Matteo Ippoliti^{2,*}, Chris Quintana¹, Ami Greene^{1,3}, Zijun Chen¹, Jonathan Gross¹, Frank Arute¹, Kunal Arya¹, Juan Atalaya¹, Ryan Babbush¹, Joseph C. Bardin^{1,4}, Joao Basso¹, Andreas Bengtsson¹, Alexander Bilmes¹, Alexandre Bourassa^{1,7}, Leon Brill¹, Michael Broughton¹, Bob B. Buckley¹, David A. Buell¹, Brian Burkett¹, Nicholas Bushnell¹, Benjamin Chiaro¹, Roberto Collins¹, William Courtney¹, Dripto Debroy¹, Sean Demura¹, Alan R. Derk¹, Andrew Dunsworth¹, Daniel Eppens¹, Catherine Erickson¹, Edward Farhi¹, Austin G. Fowler¹, Brooks Foxen¹, Craig Gidney¹, Marissa Giustina¹, Matthew P. Harrigan¹, Sean D. Harrington¹, Jeremy Hilton¹, Alan Ho¹, Sabrina Hong¹, Trent Huang¹, Ashley Huff¹, William J. Huggins¹, L. B. Ioffe¹, Sergei V. Isakov¹, Justin Iveland¹, Evan Jeffrey¹, Zhang Jiang¹, Cody Jones¹, Dvir Kafri¹, Tanuj Khattar¹, Seon Kim¹, Alexei Kitaev¹, Paul V. Klimov¹, Alexander N. Korotkov^{1,6}, Fedor Kostritsa¹, David Landhuis¹, Pavel Laptev¹, Joonho Lee^{1,8}, Kenny Lee¹, Aditya Locharla¹, Erik Lucero¹, Orion Martin¹, Jarrod R. McClean¹, Trevor McCourt¹, Matt McEwen^{1,5}, Kevin C. Miao¹, Masoud Mohseni¹, Shirin Montazeri¹, Wojciech Mruczkiewicz¹, Ofer Naaman¹, Matthew Neeley¹, Charles Neill¹, Michael Newman¹, Murphy Yuezhen Niu¹, Thomas E. O'Brien¹, Alex Opremcak¹, Eric Ostby¹, Balint Pato¹, Andre Petukhov¹, Nicholas C. Rubin¹, Daniel Sank¹, Kevin J. Satzinger¹, Vladimir Shvarts¹, Yuan Su¹, Doug Strain¹, Marco Szalay¹, Matthew D. Trevithick¹, Benjamin Villalonga¹, Theodore White¹, Z. Jamie Yao¹, Ping Yeh¹, Juhwan Yoo¹, Adam Zalcman¹, Hartmut Neven¹, Sergio Boixo¹, Vadim Smelyanskiy¹, Anthony Megrant¹, Julian Kelly¹, Yu Chen¹, S. L. Sondhi⁹, Roderich Moessner¹⁰, Kostyantyn Kechedzhi¹, Vedika Khemani², Pedram Roushan¹

¹ Google Research, Mountain View, CA, USA

² Department of Physics, Stanford University, Stanford, CA, USA

³ Department of Physics, Massachusetts Institute of Technology, Cambridge, MA, USA

⁴ Department of Electrical and Computer Engineering, University of Massachusetts, Amherst, MA, USA

⁵ Department of Physics, University of California, Santa Barbara, CA, USA

⁶ Department of Electrical and Computer Engineering, University of California, Riverside, CA, USA

⁷ Pritzker School of Molecular Engineering, University of Chicago, Chicago, IL, USA

⁸ Department of Chemistry, Columbia University, New York, NY 10027, USA

⁹ Department of Physics, Princeton University, Princeton, NJ, USA

¹⁰ Max-Planck-Institut für Physik komplexer Systeme, 01187 Dresden, Germany

* These authors contributed equally to this work.

Acknowledgements—This work was supported in part from the Defense Advanced Research Projects Agency (DARPA) via the DRINQS program (M.I., V.K., R.M., S.S.), by a Google Research Award: Quantum Hardware For Scientific Research In Physics (V.K. and M.I.), and from the Sloan Foundation through a Sloan Research Fellowship (V.K.) The views, opinions and/or findings expressed are those of the authors and should not be interpreted as representing the official views or policies of the Department of Defense or the U.S. Government. M.I. was funded in part by the Gordon and Betty Moore Foundation's EPiQS Initiative through Grant GBMF8686. This work was partly supported by the Deutsche Forschungsgemeinschaft under grants SFB 1143 (project-id 247310070) and the cluster of excellence ct.qmat (EXC 2147, project-id 390858490).

Author contributions—M.I., K.K., V.K., R.M. and S.S. conceived the project. X.M., C.Q. and P.R. executed the experiment. All the aforementioned discussed the project in progress and interpreted the results. M.I., K.K., V.K. and X.M., designed measurement protocols. J.C., A.G., J.G. and X.M. implemented and calibrated the CPHASE gates. M.I. and V.K. performed theoretical and numerical analyses. M.I., K.K., V.K., R.M., X.M., and P.R. wrote the manuscript. M.I. and X.M. wrote the supplementary material. Y.C., K.K., V.K., H.N., P.R. and V.S. led and coordinated the project. Infrastructure support was provided by Google Quantum AI. All authors contributed to revising the manuscript and the supplementary material.

Data availability—The data presented in this work are available from the corresponding authors upon reasonable request.

-
- [1] Xiao-Gang Wen, *Quantum field theory of many-body systems: from the origin of sound to an origin of light and electrons* (Oxford University Press, Oxford, 2007).
- [2] Marin Bukov, Luca D'Alessio, and Anatoli Polkovnikov, “Universal high-frequency behavior of periodically driven systems: from dynamical stabilization to floquet engineering,” *Advances in Physics* **64**, 139–226 (2015).
- [3] Fenner Harper, Rahul Roy, Mark S. Rudner, and S.L. Sondhi, “Topology and broken symmetry in floquet systems,” *Annual Review of Condensed Matter Physics* **11**, 345–368 (2020).
- [4] Takashi Oka and Hideo Aoki, “Photovoltaic hall effect in graphene,” *Physical Review B* **79** (2009), 10.1103/physrevb.79.081406.
- [5] Mark S. Rudner, Netanel H. Lindner, Erez Berg, and Michael Levin, “Anomalous edge states and the bulk-edge correspondence for periodically driven two-dimensional systems,” *Phys. Rev. X* **3**, 031005 (2013).
- [6] Paraj Titum, Erez Berg, Mark S. Rudner, Gil Refael, and Netanel H. Lindner, “Anomalous floquet-anderson insulator as a nonadiabatic quantized charge pump,” *Phys. Rev. X* **6**, 021013 (2016).
- [7] V. Khemani, A. Lazarides, R. Moessner, and S. Sondhi, “Phase structure of driven quantum systems,” *Phys. Rev.*

- Lett.* **116**, 250401 (2016).
- [8] Hoi Chun Po, Lukasz Fidkowski, Takahiro Morimoto, Andrew C. Potter, and Ashvin Vishwanath, “Chiral floquet phases of many-body localized bosons,” *Phys. Rev. X* **6**, 041070 (2016).
 - [9] Dominic V. Else, Bela Bauer, and Chetan Nayak, “Floquet time crystals,” *Phys. Rev. Lett.* **117**, 090402 (2016).
 - [10] C. W. von Keyserlingk, Vedika Khemani, and S. L. Sondhi, “Absolute stability and spatiotemporal long-range order in floquet systems,” *Phys. Rev. B* **94**, 085112 (2016).
 - [11] Krzysztof Sacha and Jakub Zakrzewski, “Time crystals: a review,” *Reports on Progress in Physics* **81**, 016401 (2017).
 - [12] V. Khemani, R. Moessner, and S. Sondhi, “A brief history of time crystals,” *arXiv e-prints*, arXiv:1910.10745 (2019).
 - [13] Patrick Bruno, “Impossibility of Spontaneously Rotating Time Crystals: A No-Go Theorem,” *Phys. Rev. Lett.* **111**, 070402 (2013), arXiv:1306.6275 [quant-ph].
 - [14] Haruki Watanabe and Masaki Oshikawa, “Absence of quantum time crystals,” *Physical Review Letters* **114** (2015), 10.1103/physrevlett.114.251603.
 - [15] David A. Huse, Rahul Nandkishore, Vadim Oganesyan, Arijeet Pal, and S. L. Sondhi, “Localization-protected quantum order,” *Phys. Rev. B* **88**, 014206 (2013).
 - [16] David Pekker, Gil Refael, Ehud Altman, Eugene Demler, and Vadim Oganesyan, “Hilbert-glass transition: New universality of temperature-tuned many-body dynamical quantum criticality,” *Phys. Rev. X* **4**, 011052 (2014).
 - [17] D.M. Basko, I.L. Aleiner, and B.L. Altshuler, “Metal-insulator transition in a weakly interacting many-electron system with localized single-particle states,” *Annals of Physics* **321**, 1126–1205 (2006).
 - [18] R. Nandkishore and D. A. Huse, “Many-body localization and thermalization in quantum statistical mechanics,” *Annu. Rev. Condens. Matter Phys.* **6**, 15–38 (2015).
 - [19] Dmitry A. Abanin, Ehud Altman, Immanuel Bloch, and Maksym Serbyn, “Colloquium: Many-body localization, thermalization, and entanglement,” *Rev. Mod. Phys.* **91**, 021001 (2019).
 - [20] Pedro Ponte, Z. Papic, Francois Huveneers, and Dmitry A. Abanin, “Many-body localization in periodically driven systems,” *Physical Review Letters* **114** (2015), 10.1103/physrevlett.114.140401.
 - [21] Achilleas Lazarides, Arnab Das, and Roderich Moessner, “Fate of many-body localization under periodic driving,” *Physical Review Letters* **115** (2015), 10.1103/physrevlett.115.030402.
 - [22] Pranjal Bordia, Henrik Luschen, Ulrich Schneider, Michael Knap, and Immanuel Bloch, “Periodically driving a many-body localized quantum system,” *Nature Physics* **13**, 460–464 (2017).
 - [23] M. Faraday, “On a peculiar class of acoustical figures; and on certain forms assumed by groups of particles upon vibrating elastic surfaces,” *Philosophical Transactions of the Royal Society of London* **121**, 299–340 (1831).
 - [24] Raymond E. Goldstein, “Coffee stains, cell receptors, and time crystals: Lessons from the old literature,” *Physics Today* **71**, 32–38 (2018), arXiv:1811.08179 [cond-mat.soft].
 - [25] Soonwon Choi, Joonhee Choi, Renate Landig, Georg Kucsko, Hengyun Zhou, Junichi Isoya, Fedor Jelezko, Shinobu Onoda, Hitoshi Sumiya, Vedika Khemani, Curt von Keyserlingk, Norman Y. Yao, Eugene Demler, and Mikhail D. Lukin, “Observation of discrete time-crystalline order in a disordered dipolar many-body system,” *Nature* **543**, 221–225 (2017).
 - [26] J. Zhang, P. W. Hess, A. Kyprianidis, P. Becker, A. Lee, J. Smith, G. Pagano, I.-D. Potirniche, A. C. Potter, A. Vishwanath, N. Y. Yao, and C. Monroe, “Observation of a discrete time crystal,” *Nature* **543**, 217–220 (2017).
 - [27] Jared Rovny, Robert L. Blum, and Sean E. Barrett, “Observation of discrete-time-crystal signatures in an ordered dipolar many-body system,” *Phys. Rev. Lett.* **120**, 180603 (2018).
 - [28] Soham Pal, Naveen Nishad, T. S. Mahesh, and G. J. Sreejith, “Temporal order in periodically driven spins in star-shaped clusters,” *Phys. Rev. Lett.* **120**, 180602 (2018).
 - [29] D. Else, B. Bauer, and C. Nayak, “Prethermal phases of matter protected by time-translation symmetry,” *Phys. Rev. X* **7**, 011026 (2017).
 - [30] Wen Wei Ho, Soonwon Choi, Mikhail D. Lukin, and Dmitry A. Abanin, “Critical time crystals in dipolar systems,” *Phys. Rev. Lett.* **119**, 010602 (2017).
 - [31] David J. Luitz, Roderich Moessner, S. L. Sondhi, and Vedika Khemani, “Prethermalization without temperature,” *Phys. Rev. X* **10**, 021046 (2020).
 - [32] Matteo Ippoliti, Kostyantyn Kechedzhi, Roderich Moessner, S. L. Sondhi, and Vedika Khemani, “Many-body physics in the NISQ era: quantum programming a discrete time crystal,” *arXiv e-prints*, arXiv:2007.11602 (2020), arXiv:2007.11602 [cond-mat.dis-nn].
 - [33] X. Mi, P. Roushan, C. Quintana, S. Mandra, J. Marshall, C. Neill, F. Arute, K. Arya, J. Atalaya, R. Babbush, *et al.*, “Information scrambling in computationally complex quantum circuits,” (2021), arXiv:2101.08870 [quant-ph].
 - [34] D. A. Abanin, W. De Roeck, W. W. Ho, and F. Huveneers, “Effective Hamiltonians, prethermalization, and slow energy absorption in periodically driven many-body systems,” *Phys. Rev. B* **95**, 014112 (2017).
 - [35] Takashi Mori, Tatsuhiko N Ikeda, Eriko Kaminishi, and Masahito Ueda, “Thermalization and prethermalization in isolated quantum systems: a theoretical overview,” *Journal of Physics B: Atomic, Molecular and Optical Physics* **51**, 112001 (2018).
 - [36] Daniel J. Yates, Alexander G. Abanov, and Aditi Mitra, “Long-lived π edge modes of interacting and disorder-free floquet spin chains,” (2021), arXiv:2105.13766 [cond-mat.str-el].
 - [37] This value of $\phi_i = -0.4$ is chosen to be small enough that a leading order high-frequency Floquet Magnus expansion to obtain \hat{H}_{eff} is a reasonable approximation (see SM).
 - [38] Sandu Popescu, Anthony J. Short, and Andreas Winter, “Entanglement and the foundations of statistical mechanics,” *Nature Physics* **2**, 754–758 (2006).
 - [39] Sheldon Goldstein, Joel L. Lebowitz, Roderich Tumulka, and Nino Zanghi, “Canonical typicality,” *Phys. Rev. Lett.* **96**, 050403 (2006).
 - [40] Jonas Richter and Arijeet Pal, “Simulating hydrodynamics on noisy intermediate-scale quantum devices with random circuits,” *Phys. Rev. Lett.* **126**, 230501 (2021).
 - [41] F. Arute, K. Arya, R. Babbush, D. Bacon, J. C. Bardin, R. Barends, R. Biswas, S. Boixo, F. G. S. L. Brand

- dao, D. A. Buell, *et al.*, “Quantum supremacy using a programmable superconducting processor,” *Nature* **574**, 505–510 (2019).
- [42] S F Edwards and P W Anderson, “Theory of spin glasses,” *Journal of Physics F: Metal Physics* **5**, 965–974 (1975).
 - [43] Jonas A. Kjäll, Jens H. Bardarson, and Frank Pollmann, “Many-body localization in a disordered quantum ising chain,” *Phys. Rev. Lett.* **113**, 107204 (2014).
 - [44] Arijeet Pal and David A. Huse, “Many-body localization phase transition,” *Phys. Rev. B* **82**, 174411 (2010).
 - [45] D.A. Abanin, J.H. Bardarson, G. De Tomasi, S. Gopalakrishnan, V. Khemani, S.A. Parameswaran, F. Pollmann, A.C. Potter, M. Serbyn, and R. Vasseur, “Distinguishing localization from chaos: Challenges in finite-size systems,” *Annals of Physics* **427**, 168415 (2021).
 - [46] B. Foxen, C. Neill, A. Dunsworth, P. Roushan, B. Chiaro, A. Megrant, J. Kelly, Z. Chen, K. Satzinger, R. Barends, *et al.* (Google AI Quantum), “Demonstrating a continuous set of two-qubit gates for near-term quantum algorithms,” *Phys. Rev. Lett.* **125**, 120504 (2020).
 - [47] Frank Arute, Kunal Arya, Ryan Babbush, Dave Bacon, Joseph C. Bardin, Rami Barends, Andreas Bengtsson, Sergio Boixo, Michael Broughton, Bob B. Buckley, *et al.*, “Observation of separated dynamics of charge and spin in the fermi-hubbard model,” (2020), [arXiv:2010.07965](https://arxiv.org/abs/2010.07965) [quant-ph].
 - [48] C. Neill, T. McCourt, X. Mi, Z. Jiang, M. Y. Niu, W. Mruczkiewicz, I. Aleiner, F. Arute, K. Arya, J. Atalaya, *et al.*, “Accurately computing the electronic properties of a quantum ring,” *Nature* **594**, 508–512 (2021).
 - [49] This is true up to single-qubit Z rotations on the edge qubits, if the chain has open boundary conditions. These could be cancelled by considering the evolution over 4 periods, with minor changes to the result (a cancellation of terms near the edges). For the sake of simplicity we will neglect this effect here.
 - [50] Christian Bartsch and Jochen Gemmer, “Dynamical typicality of quantum expectation values,” *Phys. Rev. Lett.* **102**, 110403 (2009).
 - [51] Jean Dalibard, Yvan Castin, and Klaus Mølmer, “Wave-function approach to dissipative processes in quantum optics,” *Phys. Rev. Lett.* **68**, 580–583 (1992).

Supplementary Materials for “Observation of Time-Crystalline Eigenstate Order on a Quantum Processor”

I. CPHASE GATE IMPLEMENTATION AND ERROR BENCHMARKING

An essential building block for the quantum circuits used to observe many-body localized DTC is the two-qubit gate $ZZ(\phi) = e^{-i\frac{\phi}{4}\hat{Z}_a\hat{Z}_b}$, which belongs to the more general family of Fermionic Simulation (FSIM) gates having the unitary form $\hat{U}_{\text{FSIM}}^{41}$:

$$\begin{pmatrix} 1 & 0 & 0 & 0 \\ 0 & e^{i(\Delta_++\Delta_-)} \cos \theta & -ie^{i(\Delta_+-\Delta_{-, \text{off}})} \sin \theta & 0 \\ 0 & -ie^{i(\Delta_++\Delta_{-, \text{off}})} \sin \theta & e^{i(\Delta_+-\Delta_-)} \cos \theta & 0 \\ 0 & 0 & 0 & e^{i(2\Delta_+-\phi)} \end{pmatrix}. \quad (3)$$

Here θ is the two-qubit iSWAP angle and Δ_+ , Δ_- and $\Delta_{-, \text{off}}$ are phases that can be freely adjusted by single-qubit Z -rotations. In this parametrized representation, $ZZ(\phi) = \hat{U}_{\text{FSIM}}(\theta = 0, \Delta_- = 0, \Delta_{-, \text{off}} = 0, \phi = 2\Delta_+)$, which is equivalent to a CPHASE gate with conditional-phase ϕ and a single-qubit rotation $Z(\frac{\phi}{2})$ acting on each qubit. Precise single-qubit Z -control has already been demonstrated in our previous work³³. Here, we focus on implementing CPHASE gates with a variable ϕ .

The qubits used in our experiment are superconducting transmon qubits with both tunable frequencies and tunable inter-qubit couplings. Due to the existence of higher states, a natural way to realize a CPHASE gate is to bring the $|11\rangle$ and $|02\rangle$ states of two coupled qubits close to resonance diabatically, allow the qubits to interact for a duration $\sim \frac{1}{\sqrt{8g^2 + \epsilon^2}}$, before turning off the inter-qubit coupling and ramping the qubits back to their idle configurations. Here $|0\rangle$ and $|1\rangle$ are the ground and excited states of each qubit, $|2\rangle$ is a leakage state outside the computational space, g denotes the inter-qubit coupling (between the $|10\rangle$ and $|01\rangle$ states) and ϵ is the detuning between the $|11\rangle$ and $|02\rangle$ states during interaction. A schematic for the flux pulses to realize the CPHASE gate is shown in Fig. 6a.

Figure 6b shows simulated values of leakage, namely the probability of one qubit residing in $|2\rangle$ after the CPHASE gate, as a function of ϵ and maximum value of g during interaction, g_{max} . A narrow arc-like region, corresponding to a contour $8g_{\text{max}}^2 + \epsilon^2 = \text{constant}$, can be seen from the simulation. The values of g_{max} and ϕ along this contour are shown in the upper panel of Fig. 6c, where we see a full range of $\phi \in [-2\pi, 0]$ can be achieved for absolute detuning values of $|\epsilon|/2\pi < 100$ MHz. Since the $|01\rangle$ and $|10\rangle$ states are detuned by ~ 200 MHz, their interaction remains dispersive during the CPHASE gate and therefore ensures a small iSWAP angle θ (we confirm this experimentally in the next section).

Experimentally, the leakage-minimizing value of g_{max}

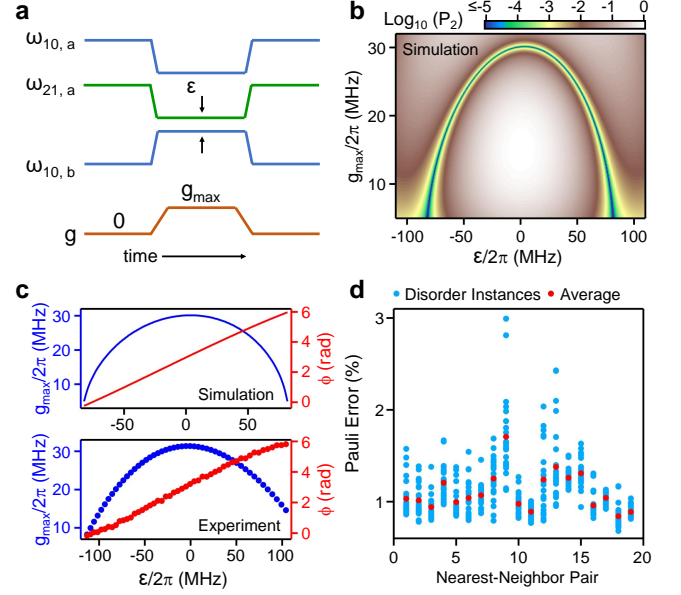


FIG. 6. Implementing CPHASE gates with tunable transmon qubits. **a**, Schematic of flux pulses used to realize a CPHASE gate. The frequencies of two coupled transmons, $\omega_{10, a}$ and $\omega_{10, b}$, are displaced from their idle positions into a configuration wherein $\omega_{10, b}$ is detuned from $\omega_{21, a}$ by an amount ϵ . At the same time, a flux pulse on the coupler turns on an inter-qubit coupling $g > 0$ with a maximum value of g_{max} for a fixed duration of ~ 18 ns. **b**, Simulated values of leakage, P_2 , as a function of ϵ and g_{max} , using typical device parameters and pulse shapes. **c**, The values of g_{max} and conditional-phase ϕ at the locations of minimum leakage, plotted for different values of ϵ . Upper panel shows simulated results and lower panel shows representative experimental values obtained from one pair of qubits. **d**, Pauli error rates for each neighboring pair of qubits in the 20-qubit chain used by the experiment, obtained from parallel XEB. Each error rate includes contributions from two random single-qubit gates ($\pi/2$ rotations around a random axis along the equatorial plane of the Bloch sphere) and a CPHASE gate. Data are shown for 24 disorder instances, with each instance including a different random set of ϕ_i across the qubit chain. Red dots show the average error of each qubit pair.

is detected for a discrete set of ϵ via $|2\rangle$ state readout and the corresponding ϕ is then calibrated using unitary tomography⁴⁶. A polynomial fit is then performed to infer values of ϵ and g_{max} for intermediate values of ϕ , thereby achieving a continuous family of CPHASE gates with fully tunable ϕ . Example experimental calibration data for ϵ , g_{max} and ϕ are included in the bottom panel of Fig. 6c. Excellent agreement with numerical results is found. The discrepancy in values of ϵ likely arises from deviation between the actual pulse shapes on the quantum processor and those used in the numerical simula-

tion.

To estimate the errors of typical CPHASE gates, we perform cross-entropy benchmarking (XEB) similar to previous works^{33,41}. Here the gates are characterized in parallel and therefore include errors arising from any cross-talk effects. The XEB results for 24 random combinations of ϕ_i across the 20-qubit chain used in the main text are shown in Fig 6d, where we have used the so-called “cycle” Pauli error as the metric. A cycle Pauli error includes errors from two single-qubit gates and a single CPHASE gate. In computing the XEB fidelities, we have also assumed the CPHASE gate with the calibrated ϕ as the ideal gate³³. As such, the Pauli errors include contributions from both incoherent effects such as qubit relaxation and dephasing, as well as coherent effects such as any mis-calibration in ϕ and residual values of θ . The error rates are observed to be relatively dependent on ϕ , a likely consequence of changes in coherent and incoherent errors when the pulse parameters are varied. Overall, we observe an average error rate of 0.011, comparable to gates used in our past works^{33,41}.

II. FLOQUET CALIBRATION OF CPHASE GATES

After basic pulse-level calibration of CPHASE gates, the $ZZ(\phi)$ gate is then calibrated using the technique of Floquet calibration^{47,48}. Floquet calibration utilizes periodic circuits which selectively amplify different parameters within \hat{U}_{FSIM} , allowing for sensitive detection and rectification of small coherent errors for such quantum gates. Our past works have primarily focused on calibrating the iSWAP-like family of gates, where $\theta \gg \phi$. For ZZ gates, the opposite limit $\phi \gg \theta$ is true and the optimal calibration circuits are in some cases different from our previous works. In this section, we present the gate sequences and example calibration results for the ZZ gates. For a detailed description of the underlying theory of Floquet calibration, the reader is directed to our previous publications^{47,48}.

A. Calibration of Δ_+ , Δ_- and ϕ

The calibration circuits for Δ_- are illustrated in Fig. 7a and comprise two Ramsey-like measurements: Each qubit is separately initialized along the x-axis of the Bloch sphere, $|X\rangle$. A total number of d FSIM gates are then applied, which in general rotate the excited qubit around the z-axis of the Bloch sphere due to non-zero single-qubit phases within the uncalibrated \hat{U}_{FSIM} . At the end of the sequence, a Z gate with a rotation angle ξ is applied to the excited qubit, followed by a \sqrt{Y} gate. The resulting $|1\rangle$ state population, P_1 , is then measured. Example data for P_1 of each qubit are shown in the bottom panel of Fig. 7a, which are fitted to a cosine function $P_1 = B_0 + B_1 \cos(\xi + \xi_0)$ where B_0 , B_1 and ξ_0 are fit-

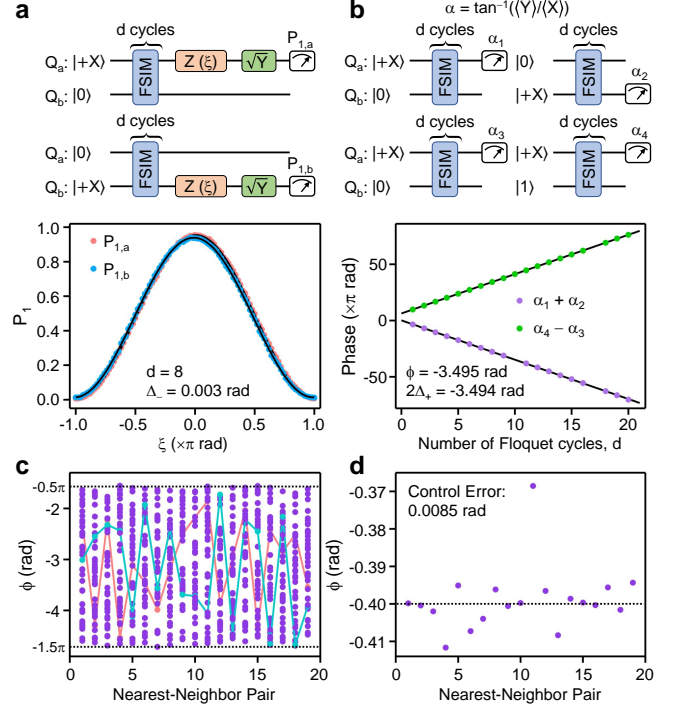


FIG. 7. Floquet calibration of single-qubit and conditional phases for CPHASE-like gates. **a**, Top panel: Gate sequences for calibrating the Δ_- angle of the FSIM. Bottom panel: Example experimental data for $P_{1,a}$ and $P_{1,b}$ ($|1\rangle$ state population for qubits Q_a and Q_b , respectively) as functions of ξ . The circuit depth is fixed at $d = 8$. Solid black lines show fits to a cosine function for each qubit, which allow Δ_- to be extracted. **b**, Top panel: Gate sequences for calibrating Δ_+ and ϕ . For each of the 4 gate sequences, the $\langle \hat{X} \rangle$ and $\langle \hat{Y} \rangle$ projections of the Bloch vector for a given qubit are measured at the end, from which an angle $\alpha = \tan^{-1}(\langle \hat{Y} \rangle / \langle \hat{X} \rangle)$ is computed. Bottom panel: Example experimentally obtained phase sums ($\alpha_1 + \alpha_2$) and differences ($\alpha_4 - \alpha_3$) as functions of d , number of cycles in the Floquet gate sequences. Solid black lines show linear fits, the slopes of which determine ϕ and Δ_+ . **c**, Experimentally measured ϕ for each neighboring pair of qubits in the 20-qubit chain. Results from 40 disorder instances are plotted. The blue and red connected dots indicate the values of two particular instances, while all other instances are shown as disconnected purple dots. Dashed lines corresponding to $\phi = -0.5\pi$ and $\phi = -1.5\pi$. **d**, Experimental measurements of ϕ when a target value is set at -0.4 (dashed line) for all nearest-neighbor pairs. An average deviation of 0.0085 rad is found between the target and measured values of ϕ .

ting parameters. The value of Δ_- is then equal to $\frac{\xi_a - \xi_b}{2d}$, where ξ_a (ξ_b) is the fitted ξ_0 for Q_a (Q_b). This equivalence may be understood through the fact that $2\Delta_-$ is the difference in the degree of local Z rotations undergone by each qubit after the application of one FSIM gate between them.

The phases Δ_+ and ϕ are calibrated using four periodic circuits sharing a similar structure, as indicated in the

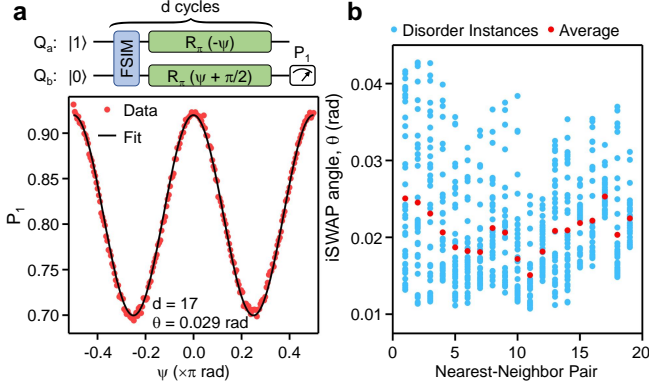


FIG. 8. **Floquet calibration of small iSWAP angles.** **a**, Top: Periodic circuit for calibrating θ : Each cycle includes an FSIM gate, followed by two single-qubit rotations $R_\pi(-\psi)$ and $R_\pi(\psi + \pi/2)$. After d cycles, the excited state population P_1 of Q_b is measured. Bottom: Example experimental data at a fixed depth $d = 17$, showing P_1 as a function of ψ . Solid black line shows fit to a sinusoidal function, the amplitude of which determines the value of θ . **b**, Experimentally measured θ for each neighboring pair of qubits in the 20-qubit chain. Results from 40 disorder instances are plotted as blue dots, and the average value for each qubit pair is plotted as red dots. Overall, θ has a mean value of 0.022 rad and a standard deviation 0.014 across all qubit pairs and disorder instances.

top panel of Fig. 7b. For Δ_+ , we again separately prepare each qubit in the $|X\rangle$ state while leaving the other qubit in $|0\rangle$. The FSIM gate is then applied d times. At the end of the sequence, two tomographic measurements are performed on the excited qubit to determine the angle of its Bloch vector, $\alpha = \tan^{-1}(\langle \hat{Y} \rangle / \langle \hat{X} \rangle)$. The total accumulated phase $\alpha_1 + \alpha_2$, where α_1 (α_2) is α for Q_a (Q_b), is equivalent to $2d\Delta_+$. This equivalence arises from the fact that $2\Delta_+$ physically corresponds to the sum of the degrees of local Z rotations on both qubits after the application of one FSIM gate.

The conditional-phase ϕ is calibrated by preparing one qubit (Q_a) in $|X\rangle$ and comparing α when the other qubit (Q_b) is initialized in either the $|0\rangle$ or the $|1\rangle$ state. A non-zero ϕ will cause the two angles, α_3 and α_4 , to differ by an amount $\alpha_4 - \alpha_3 = -d\phi$ ⁴⁶. Example experimental values of $\alpha_1 + \alpha_2$ and $\alpha_4 - \alpha_3$ as a function of d are shown in the bottom panel of Fig. 7b. The slopes of both data sets allow Δ_+ and ϕ to be extracted, which are seen to be very close to the target condition $2\Delta_+ = \phi$. Figure 7c shows experimentally calibrated values of ϕ across the 20-qubit chain, for a total of 40 disorder instances. It can be seen that ϕ falls within the intended range of $[-0.5\pi, -1.5\pi]$. Figure 7d shows the calibrated values of ϕ when each ϕ_i has a target value of -0.4 . Comparing the measured values of ϕ with the target value, we find a small control error of 0.0085 rad for ϕ .

B. Calibration of θ

For iSWAP-like gates within the FSIM family, the iSWAP angle θ can be accurately calibrated by setting $\Delta_- = 0$ and applying FSIM gates in succession, which leads to population transfer between the two qubits (initialized in $|10\rangle$) with a period of $\frac{\pi}{\theta}$. Discrete fourier transform of qubit populations therefore allow θ to be determined with very high precision⁴⁸. However, CPHASE-like gates typically have small iSWAP angles and such a technique is no longer as effective, since the period for one population transfer can be very long and the calibration data are complicated by noise effects.

To circumvent such a problem, we have designed a new gate sequence for calibrating small values of θ : Let us consider the composite unitary $\hat{U}_{\text{COM}} = \hat{U}_{\text{FSIM}} X_a Y_b$ where X_a and Y_b are X and Y π -rotations of Q_a and Q_b , respectively. \hat{U}_{COM} has the following matrix form:

$$\begin{pmatrix} 0 & 0 & 0 & -i \\ 0 & -e^{-i\Delta_{-, \text{off}}} \sin \theta & i \cos \theta & 0 \\ 0 & -i \cos \theta & e^{i\Delta_{-, \text{off}}} \sin \theta & 0 \\ ie^{-i\phi} & 0 & 0 & 0 \end{pmatrix}. \quad (4)$$

Here we have set Δ_- and Δ_+ to 0 for simplicity (non-zero values of these phases will not affect the calibration scheme discussed below). With simple algebra, it can be seen that for qubits initialized in the $|10\rangle$ state, the excited state population of Q_b after applying \hat{U}_{COM} d times (d being odd) is bounded by two values: For $\Delta_{-, \text{off}} = 0$, $P_1 = \cos^2 \theta \approx 1$ for small values of θ . For $\Delta_{-, \text{off}} = \frac{\pi}{2}$, $P_1 = \cos^2(d\theta)$. The difference between these two values is $\cos^2 \theta - \cos^2(d\theta)$ which is approximately $\sin^2(d\theta)$ for $\theta \approx 0$. As such, varying $\Delta_{-, \text{off}}$ and measuring the peak-to-peak amplitude of P_1 allows determination of θ . Compared to the fourier-transform technique, the method here requires relatively short circuit depth, as a iSWAP angle of 0.02 rad would yield a peak-to-peak amplitude of 0.1 in P_1 for $d = 17$, which can be resolved with a relatively small number of single-shot measurements.

The experimental Floquet circuit for calibrating θ is shown in the upper panel of Fig. 8a. Here, we have injected a variational angle ψ into the single-qubit π -rotations. Varying ψ effectively changes χ of the FSIM gate. The experimental calibration data for a given pair of qubits are shown in the bottom panel of Fig. 8a, where we see oscillations of P_1 as a function of ψ . Fitting the data to a sinusoidal function allows a peak-to-peak amplitude of 0.22 to be determined, which corresponds to a iSWAP angle of $\theta = 0.029$ rad.

The iSWAP angles for all qubit pairs of the 20-qubit chain are shown in Fig. 8b, where we have included data for 40 disorder instances in ϕ . A small average value of 0.022 rad is found for the qubit chain, with the fluctuation between disorder instances understood as a result of different detunings between the $|01\rangle$ and $|10\rangle$ states during the flux pulses of different gates.

III. DERIVATION OF EFFECTIVE HAMILTONIANS

The bit-string energies shown in the inset to Fig. 3b are based on effective Hamiltonians \hat{H}_{eff} that, in certain limits, approximate the effect of the unitary circuit over two periods, $\hat{U}_F^2 \approx e^{-2i\hat{H}_{\text{eff}}}$. Here we derive the relevant \hat{H}_{eff} operators for the models in Fig. 3b.

A. Uniform $\phi_i = -0.4$

For the model with uniform CPHASE angles $\phi_i \equiv \bar{\phi} = -0.4$ and random single-qubit Z rotation angles $h_i \in [-\pi, \pi]$, a period of the time evolution is represented by

$$\hat{U}'_F = \hat{U}_z[\bar{\phi}, \mathbf{h}] \hat{U}_x[\pi - 2\epsilon] \quad (5)$$

with

$$\begin{aligned} \hat{U}_x[\theta] &= e^{-i\frac{\theta}{2} \sum_n \hat{X}_n}, \\ \hat{U}_z[\bar{\phi}, \mathbf{h}] &= e^{-i \sum_n (\bar{\phi}/4) \hat{Z}_n \hat{Z}_{n+1} + (h_n/2) \hat{Z}_n}. \end{aligned}$$

We have also defined the detuning $\epsilon = \frac{\pi}{2}(1 - g)$; in the following we take $\epsilon \ll 1$, i.e. g close to 1. The evolution over two periods is given by

$$\begin{aligned} (\hat{U}'_F)^2 &= \hat{U}_z[\bar{\phi}, \mathbf{h}] \hat{U}_x[\pi - 2\epsilon] \hat{U}_z[\bar{\phi}, \mathbf{h}] \hat{U}_x[\pi - 2\epsilon] \\ &= \hat{U}_z[\bar{\phi}, \mathbf{h}] \hat{U}_x[-2\epsilon] \hat{U}_z[\bar{\phi}, -\mathbf{h}] \hat{U}_x[-2\epsilon] \end{aligned} \quad (6)$$

where we have used the commutation properties of the perfect π pulse $\hat{U}_x[\pi] = \prod_n \hat{X}_n$. Next, we note that $\hat{U}_z[\bar{\phi}, -\mathbf{h}] = \hat{U}_z[\bar{\phi}, 0] \hat{U}_z[0, \mathbf{h}]^\dagger$; acting by conjugation with $\hat{U}_z[0, \mathbf{h}]$ on $\hat{U}_x[-2\epsilon]$ gives

$$(\hat{U}'_F)^2 = \hat{U}_z[\bar{\phi}, 0] e^{i\epsilon \sum_n \cos(h_n) \hat{X}_n + \sin(h_n) \hat{Y}_n} \hat{U}_z[\bar{\phi}, 0] \hat{U}_x[-2\epsilon]. \quad (7)$$

The effective Hamiltonian \hat{H}_{eff} , satisfying $(\hat{U}'_F)^2 \approx e^{-2i\hat{H}_{\text{eff}}}$, is then given to leading order in ϵ , $|\bar{\phi}/4| \ll 1$ via the Baker-Campbell-Hausdorff (BCH) formula:

$$\begin{aligned} \hat{H}_{\text{eff}} &= \sum_n \frac{\epsilon}{2} [(1 + \cos(h_n)) \hat{X}_n + \sin(h_n) \hat{Y}_n] + \\ &\quad + \frac{\bar{\phi}}{4} \hat{Z}_n \hat{Z}_{n+1}. \end{aligned} \quad (8)$$

Thus, for any bit-string $\mathbf{s} \in \{0, 1\}^L$, the energy of the associated computational basis state $|\mathbf{s}\rangle = |s_1\rangle |s_2\rangle \cdots |s_L\rangle$ is

$$E_{\mathbf{s}} = \langle \mathbf{s} | \hat{H}_{\text{eff}} | \mathbf{s} \rangle = \frac{\bar{\phi}}{4} \sum_n (-1)^{s_n + s_{n+1}}, \quad (9)$$

which simply counts the number of “domain walls” (i.e. bonds where $s_i \neq s_{i+1}$) in \mathbf{s} . Thus the polarized and staggered bit-strings (having 0 and $L-1$ “domain walls”,

respectively) lie near the edges of the spectrum in all realizations.

We note that, strictly speaking, a prethermal DTC requires \hat{H}_{eff} to have a symmetry breaking transition at a finite critical temperature T_c . In this case, ordered initial states at temperatures $T < T_c$ show long-lived oscillations with an amplitude that depends on the equilibrium value of the (symmetry breaking) order parameter at temperature T ²⁹. As short-ranged models in one dimension (such as the one under consideration) cannot have order at finite temperature, this model is not prethermal in the sense we just described. However, thermal correlation lengths may still exceed the size of the system when the latter is small enough. This allows low-temperature states of \hat{H}_{eff} to show long-lived oscillations with a finite amplitude, even if the equilibrium order parameter is asymptotically zero for such states.

B. Disordered $\phi_i \in [-1.5\pi, -0.5\pi]$

In the MBL DTC drive \hat{U}_F we set the average CPHASE angle to $\bar{\phi} = -\pi$, which (being ~ 10 times larger than in the previous case) breaks the final step in the derivation of Eq. (8). We can however use another approach, valid if $\phi_i = -\pi + \delta\phi_i$, with $|\delta\phi_i|$ sufficiently small. In Eq. (7) we replace $\bar{\phi}$ by $\pi + \delta\phi$, and noting that $\hat{U}_z[\pi, 0] = \hat{U}_z[-\pi, 0]$ ⁴⁹ we have

$$\begin{aligned} \hat{U}_F^2 &= \hat{U}_z[\delta\phi, 0] e^{i\epsilon \sum_n (\cos(h_n) \hat{Y}_n - \sin(h_n) \hat{X}_n) (\hat{Z}_{n-1} + \hat{Z}_{n+1})} \\ &\quad \times \hat{U}_z[\delta\phi, 0] \hat{U}_x[-2\epsilon]. \end{aligned} \quad (10)$$

If $\epsilon, |\delta\phi_i| \ll 1$, leading-order BCH yields

$$\begin{aligned} \hat{H}_{\text{eff}} &= \sum_n \frac{\epsilon}{2} [\hat{X}_n + \cos(h_n) \hat{Y}_n (\hat{Z}_{n-1} + \hat{Z}_{n+1})] \\ &\quad + \frac{\delta\phi_n}{4} \hat{Z}_n \hat{Z}_{n+1} - \frac{\epsilon}{2} \sin(h_n) \hat{X}_n (\hat{Z}_{n-1} + \hat{Z}_{n+1}) \end{aligned} \quad (11)$$

The energy of a bit-string state $|\mathbf{s}\rangle$ is

$$E_{\mathbf{s}} = \langle \mathbf{s} | \hat{H}_{\text{eff}}^{(0)} | \mathbf{s} \rangle = \sum_n \frac{\delta\phi_n}{4} (-1)^{s_n + s_{n+1}}. \quad (12)$$

Unlike the result in Eq. (9), this does not single out special bit-strings. More specifically, under disorder averaging all bit-strings have the same energy: $\overline{E_{\mathbf{s}}} = 0$.

In our model, the $|\delta\phi_i|$ angles are not small (they vary in $[-0.5\pi, 0.5\pi]$) so all orders in BCH should be included for an accurate result – the above is only meant to be a qualitative approximation. Nevertheless, the independence of (disorder-averaged) quantities from the choice of bit-string can be proven exactly for this model.

All bit-string states are obtained as $|\mathbf{s}\rangle = \hat{X}_{\mathbf{s}} |\mathbf{0}\rangle$, where $|\mathbf{0}\rangle = |00 \dots 00\rangle$ is the polarized state and $\hat{X}_{\mathbf{s}} = \prod_{i:s_i=1} \hat{X}_i$ flips the qubits where $s_i = 1$. We will show that all bit-string states give rise to the same dynamics as the polarized one, up to a change in the realization of

disorder. Indeed, the change of basis that maps $|\mathbf{s}\rangle$ to $|\mathbf{0}\rangle$ acts on \hat{U}_F as

$$\hat{X}_{\mathbf{s}}\hat{U}_F\hat{X}_{\mathbf{s}} = \hat{U}_z[\phi', \mathbf{h}']\hat{U}_x[\pi g] \quad (13)$$

where $\phi'_i = (-1)^{s_i+s_{i+1}}\phi_i$ and $h'_i = (-1)^{s_i}h_i$. ϕ' and \mathbf{h}' almost define another valid realization of disorder, except that wherever $s_i \neq s_{i+1}$, we have $\phi'_i \in [0.5\pi, 1.5\pi]$ (as opposed to $\phi_i \in [-1.5\pi, -0.5\pi]$). This can be remedied by setting $\phi''_i = \phi'_i - 2\pi \in [-1.5\pi, -0.5\pi]$, and noting that $e^{-i\frac{\pi}{2}\hat{Z}_i\hat{Z}_{i+1}} \propto e^{-i\frac{\pi}{2}\hat{Z}_i}e^{-i\frac{\pi}{2}\hat{Z}_{i+1}}$, so that the excess 2π CPHASE angle can be transferred to single-qubit rotations: $\hat{U}_z[\phi', \mathbf{h}'] \propto \hat{U}_z[\phi'', \mathbf{h}'']$, where $h''_i = h'_i$ if $s_{i-1} = s_{i+1}$, or $h'_i + \pi$ otherwise. Thus the dynamics of bit-string $|\mathbf{s}\rangle$ under disorder realization (ϕ, \mathbf{h}) is mapped to the dynamics of $|\mathbf{0}\rangle$ under a different realization (ϕ'', \mathbf{h}'') . Further, the mapping between realizations conserves the (uniform) measure over the intervals $\phi_i \in [-1.5\pi, -0.5\pi]$, $h_i \in [-\pi, \pi]$. Thus after averaging over disorder, all bit-strings are equivalent to each other.

IV. ECHO CIRCUIT FOR NOISE MITIGATION

The “echo” circuit \hat{U}_{ECHO} used to define the normalization A_0 in Fig. 2c and Fig. 4d of the main text consists of t steps of forward time evolution under \hat{U}_F and t steps for “backward” time evolution under \hat{U}_F^\dagger . In the absence of noise, the two cancel exactly. Thus deviations from this outcome quantify the impact of noise.

A. Circuit inversion

Our device allows the calibration of a continuous family of CPHASE angles on each bond and their use during a single circuit run. Thus it is possible to concatenate the forward and backward time evolutions \hat{U}_F and $(\hat{U}_F^\dagger)^t$ directly. However, the two-qubit gates in \hat{U}_F^\dagger would have in general different fidelity than those in \hat{U}_F . As a result, the decoherence during \hat{U}_{ECHO} would differ from that during \hat{U}_F .

To circumvent this, we effectively invert the circuit \hat{U}_F without changing the two-qubit gates, thus keeping the fidelity unchanged during the backward time evolution. The key idea is to apply X rotations on even qubits, $\hat{P}_{\pi,e} \equiv \prod_{n=1}^{L/2} \hat{X}_{2n}$, before and after each period of the circuit that is to be inverted. Indeed conjugating \hat{U}_F by $\hat{P}_{\pi,e}$ changes the sign of all ϕ_n CPHASE angles. It also changes the sign of single-qubit Z rotation angles h_n on even sites. The sign of remaining h_n fields and of g , as well as the relative order of the X and Z parts of the drive, can be changed at the level of single-qubit gates, with minor effects on fidelity.

In practice, after t cycles of \hat{U}_F , we apply the single-qubit rotations $\hat{P}_{\pi,e}$ only once, and then switch to a unitary \hat{V}_F which has the same 2-qubit gates as \hat{U}_F but different single-qubit gates chosen so that $\hat{P}_{\pi,e}\hat{V}_F\hat{P}_{\pi,e} = \hat{U}_F^\dagger$

(as explained above). Finally we measure in the computational basis and flip the logical value of all bits at even positions (this is equivalent to acting with $\hat{P}_{\pi,e}$ at the final time but avoids any fidelity losses). This way, we manage to effectively invert the circuit without altering two-qubit gate fidelities.

B. Measuring the effect of decoherence

Let us model noise as a single-qubit channel

$$\mathcal{E}_p = \left(1 - \frac{4p}{3}\right) \mathcal{I} + \frac{4p}{3} \mathcal{D} \quad (14)$$

where \mathcal{I} is the identity channel ($\mathcal{I}(\hat{\rho}) = \hat{\rho}$), \mathcal{D} is the single-qubit erasure channel ($\mathcal{D}(\hat{\rho}) \propto I$), and p denotes the error rate. We assume the noise acts symmetrically before and after each iteration of the unitary circuit (while realistically noise acts *during* the entire evolution, this is a good approximation as long as $p \ll 1$). Then the time evolution of the system over a period is described by a quantum channel

$$\hat{\rho} \mapsto \mathcal{E}_{p/2}^{\otimes L} \circ \mathcal{U}_F \circ \mathcal{E}_{p/2}^{\otimes L}(\hat{\rho}) \equiv \Phi(\hat{\rho}) \quad (15)$$

where $\mathcal{U}_F(\hat{\rho}) = \hat{U}_F\hat{\rho}\hat{U}_F^\dagger$. Similarly the inverted time evolution is given by

$$\hat{\rho} \mapsto \mathcal{E}_{p/2}^{\otimes L} \circ \mathcal{U}_F^\dagger \circ \mathcal{E}_{p/2}^{\otimes L}(\hat{\rho}) \equiv \Phi^\dagger(\hat{\rho}) \quad (16)$$

where $\mathcal{U}_F^\dagger(\hat{\rho}) = \hat{U}_F^\dagger\hat{\rho}\hat{U}_F$, and the last equality holds because \mathcal{E}_p is self-adjoint. The entire echo circuit sequence is thus described by the channel $(\Phi^\dagger)^t \circ \Phi^t$. The expectation value of \hat{Z}_i after the circuit is given by

$$\langle \hat{Z}_i \rangle_{\mathbf{s}}^{\text{echo}} \equiv \text{Tr} \left(\hat{Z}_i (\Phi^\dagger)^t \circ \Phi^t (|\mathbf{s}\rangle \langle \mathbf{s}|) \right) \quad (17)$$

The temporal autocorrelator between \hat{Z}_i before and after the echo circuit is simply $(-1)^{s_i} \langle \hat{Z}_i \rangle_{\mathbf{s}}^{\text{echo}}$. Averaging over all bit-strings yields

$$\begin{aligned} A_0^2 &\equiv \frac{1}{2^L} \sum_{\mathbf{s}} (-1)^{s_i} \langle \hat{Z}_i \rangle_{\mathbf{s}}^{\text{echo}} \\ &= \frac{1}{2^L} \sum_{\mathbf{s}} \text{Tr} \left[\hat{Z}_i (\Phi^\dagger)^t \circ \Phi^t (\hat{Z}_i |\mathbf{s}\rangle \langle \mathbf{s}|) \right] \\ &= \frac{1}{2^L} \text{Tr} \left[(\Phi^t(\hat{Z}_i))^2 \right] = \|\Phi^t(\hat{Z}_i)\|^2 / \|\hat{Z}_i\|^2, \end{aligned} \quad (18)$$

where we have used the definition of adjoint channel, $(\hat{V}, \Phi(\hat{W})) = (\Phi^\dagger(\hat{V}), \hat{W})$, relative to the trace inner product $(\hat{V}, \hat{W}) = \text{Tr}(\hat{V}^\dagger \hat{W})$. Thus from the protocol outlined above one extracts the decay of operator norm $\|\hat{Z}_i(t)\| \sim A_0 \|\hat{Z}_i(0)\|$ which is the leading effect of decoherence. The ratio A/A_0 in Fig. 7d thus gives the overlap between *normalized* operators,

$$\frac{A}{A_0} = \left(\frac{\langle \hat{Z}_i(0) | \hat{Z}_i(t) \rangle}{\|\hat{Z}_i(0)\| \|\hat{Z}_i(t)\|} \right). \quad (19)$$

V. SPECTRAL AVERAGES VIA QUANTUM TYPICALITY

Quantum typicality^{38,39,50} states that, for any observable \hat{O} in a Hilbert space of dimension 2^L , the expectation value $\langle \hat{O} \rangle_\psi$ on a *random state* ψ sampled from the unitarily invariant (Haar) measure obeys these statistical properties:

$$\mathbb{E}_\psi \langle \hat{O} \rangle_\psi = \langle \hat{O} \rangle_\infty \quad (20)$$

$$\text{Var}_\psi \langle \hat{O} \rangle_\psi = \frac{1}{2^L + 1} \left(\langle \hat{O}^2 \rangle_\infty - \langle \hat{O} \rangle_\infty^2 \right) \quad (21)$$

where $\langle \hat{O} \rangle_\infty \equiv 2^{-L} \text{Tr}(\hat{O})$ denotes the expectation value on the infinite-temperature state. Thus for large L , the matrix element $\langle \hat{O} \rangle_\psi$ is distributed as a Gaussian centered at the infinite-temperature value with an extremely narrow standard deviation, $\simeq 2^{-L/2}$, which enables the measurement of spectrally-averaged quantities with exponentially high accuracy from a single pure state.

A. Scrambling circuit and approach to typicality

In the main text we report data on spectrally-averaged autocorrelators $\langle \hat{Z}_i(0) \hat{Z}_i(t) \rangle_\infty$ obtained with a method based on the idea above, i.e by evaluating $\langle \hat{Z}_i(0) \hat{Z}_i(t) \rangle_\psi$ on a state $|\psi\rangle$ which is close to typical random states in the Hilbert space. In order to prepare a random state $|\psi\rangle$, we start with a bit-string state and evolve it via a scrambling circuit \hat{U}_S , as also proposed in Ref.⁴⁰. This consists of K layers of CZ gates (CPHASE with angle $\phi = \pi$) and random single-qubit gates (rotations around a random direction on the XY plane by an angle θ sampled uniformly in $[0.4\pi, 0.6\pi]$). The single-qubit gates vary randomly in both space and time, so that \hat{U}_S is not a Floquet circuit. After a number of layers $K = O(L)$ (we neglect decoherence for now), the prepared state $|\psi\rangle = \hat{U}_S |\mathbf{s}\rangle$ behaves like typical random vectors in the Hilbert space, so that $\langle \psi | \hat{O} | \psi \rangle = \langle \hat{O} \rangle_\infty + \delta$, where the error δ (a random variable dependent on the choice of bit-string \mathbf{s} and of scrambling circuit \hat{U}_S) has zero mean and variance $\sim 2^{-\min(L, cK)}$ for some constant $c > 0$, i.e., the variance shrinks with increasing K as the state becomes gradually more random, until it saturates to the quantum typicality result Eq. (21). In Fig. 9a we show the results of exact numerical simulations that confirm this picture. For this family of random circuits, we find $c \simeq 0.36$ (from a fit to the data in the inset to Fig. 9a).

B. Ancilla protocol

To measure two-time correlators $\langle \psi | \hat{Z}_i(0) \hat{Z}_i(t) | \psi \rangle$ in the “pseudorandom states” $|\psi\rangle$ defined above, we use an interferometric protocol similar to the one employed in Ref.³³. We introduce an ancilla qubit initialized in state

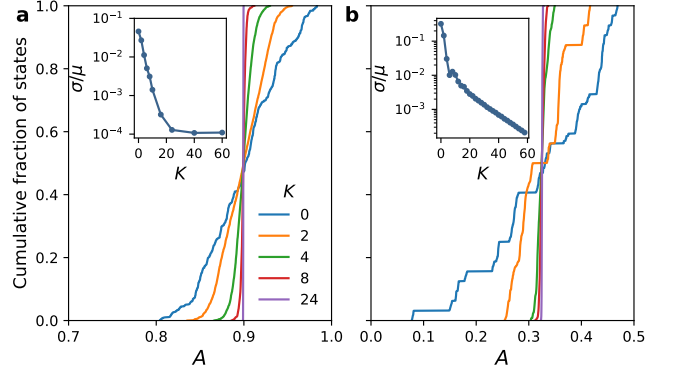


FIG. 9. **Simulation of quantum typicality protocol.** **a**, Cumulative distribution of autocorrelators A from a set of 2000 bit-string states pre-processed by a depth- K random circuit \hat{U}_S as described in the text, for variable K . We set $g = 0.94$ (MBL DTC phase). The realization of disorder is fixed and A is computed at time $t = 30$ on qubit Q_{11} in a chain of $L = 20$ qubits. Inset: relative standard deviation σ/μ decreases exponentially in K and approaches the random-state variance ($< 2^{-L/2}$) after depth $K \simeq L$. **b**, Same plot for noisy simulations (depolarizing noise, error rate $p = 0.5\%$ per 2-qubit gate, exact density matrix simulations) of qubit Q_7 in a chain of $L = 12$ qubits, where we include all 4096 bit-string states. Inset: relative standard deviation σ/μ . σ decreases indefinitely with K due to decoherence, while μ is not affected.

$|+X\rangle = (|0\rangle + |1\rangle)/\sqrt{2}$ alongside the system qubits Q_1, \dots, Q_L which are initialized in a bit-string state $|\mathbf{s}\rangle$. We evolve the system qubits with the scrambling circuit \hat{U}_S for depth K , obtaining a joint state $|\psi\rangle_{\text{sys}} |+X\rangle_{\text{a}}$. Then we apply a CZ gate between the ancilla and system qubit i , so that the state “branches” into the superposition

$$\frac{1}{\sqrt{2}} \left(|\psi\rangle_{\text{sys}} |0\rangle_{\text{a}} + \hat{Z}_i |\psi\rangle_{\text{sys}} |1\rangle_{\text{a}} \right) \quad (22)$$

We then evolve the system under the Floquet drive \hat{U}_F for t periods and again apply a CZ between the ancilla and system qubit i , which gives

$$\frac{1}{\sqrt{2}} \left(\hat{U}_F^t |\psi\rangle_{\text{sys}} |0\rangle_{\text{a}} + \hat{Z}_i \hat{U}_F^t \hat{Z}_i |\psi\rangle_{\text{sys}} |1\rangle_{\text{a}} \right) \quad (23)$$

Finally, we measure the ancilla in the X basis. The expectation value of the measurement is

$$\begin{aligned} \langle \hat{X}_{\text{a}} \rangle &= \frac{1}{2} \langle \psi | \hat{U}_F^{-t} \hat{Z}_i \hat{U}_F^t \hat{Z}_i | \psi \rangle + \text{c.c.} \\ &= \text{Re} \langle \psi | \hat{Z}_i(t) \hat{Z}_i(0) | \psi \rangle \\ &\simeq \langle \hat{Z}_i(0) \hat{Z}_i(t) \rangle_\infty \end{aligned} \quad (24)$$

where the last line follows from quantum typicality if $|\psi\rangle$ is random. On a sufficiently large system, and for large enough K (number of scrambling cycles), this protocol gives the spectrum-averaged temporal autocorrelator from a single measurement.

C. Effect of noise during the scrambling circuit

The above discussion neglects decoherence and treats the states during the protocol as pure. Since K must grow with L for the protocol to succeed, it is especially important to understand whether noise during the random state preparation process has a negative impact on the result.

One can repeat the previous discussion with quantum channels instead of unitary operators: the system starts in pure state $|\mathbf{s}\rangle\langle\mathbf{s}|_{\text{sys}}|+\mathbf{X}\rangle\langle+\mathbf{X}|_{\text{a}}$ and evolves under the scrambling dynamics into $\hat{\rho}_{\text{sys}}|+\mathbf{X}\rangle\langle+\mathbf{X}|_{\text{a}}$, where $\hat{\rho} = \Phi_S(|\mathbf{s}\rangle\langle\mathbf{s}|)$ and Φ_S is a quantum channel representing the noisy version of the scrambling circuit \hat{U}_S (we neglect decoherence on the ancilla qubit). The protocol then proceeds analogously to the noiseless case and yields the final state

$$\begin{aligned} \hat{\rho}'_{\text{sys,a}} = & \frac{1}{2} [\Phi^t(\hat{\rho})_{\text{sys}} |0\rangle\langle 0|_{\text{a}} + (\hat{Z}_i \Phi^t(\hat{Z}_i \hat{\rho}))_{\text{sys}} |1\rangle\langle 0|_{\text{a}} \\ & + (\Phi^t(\hat{\rho} \hat{Z}_i) \hat{Z}_i)_{\text{sys}} |0\rangle\langle 1|_{\text{a}} \\ & + (\hat{Z}_i \Phi^t(\hat{Z}_i \hat{\rho} \hat{Z}_i) \hat{Z}_i)_{\text{sys}} |1\rangle\langle 1|_{\text{a}}] \end{aligned} \quad (25)$$

where Φ is the noisy version of the Floquet evolution \hat{U}_F . The expectation of \hat{X}_{a} on this state is

$$\begin{aligned} \langle \hat{X}_{\text{a}} \rangle &= \frac{1}{2} \text{Tr} [\hat{Z}_i \Phi^t(\hat{Z}_i \hat{\rho}) + \Phi^t(\hat{\rho} \hat{Z}_i) \hat{Z}_i] \\ &= \frac{1}{2} \text{Tr} [\{\hat{Z}_i(t), \hat{Z}_i(0)\} \hat{\rho}] \end{aligned} \quad (26)$$

where we have defined $\hat{Z}_i(t) = (\Phi^\dagger)^t[\hat{Z}_i]$ as the Heisenberg-picture evolution of \hat{Z}_i with noise.

To see that Eq. (26) approximates the infinite-temperature expectation value $\langle \hat{Z}_i(0) \hat{Z}_i(t) \rangle_\infty$, we observe that under a random unitary circuit, noise can be approximated by a global depolarizing channel⁴¹: $\Phi_S(|\mathbf{s}\rangle\langle\mathbf{s}|) \approx f^K \hat{U}_S |\mathbf{s}\rangle\langle\mathbf{s}| \hat{U}_S^\dagger + (1 - f^K) \hat{I}/2^L$, i.e. a sum of the ideal evolution under \hat{U}_S and the fully mixed state $\hat{I}/2^L$ (\hat{I} is the identity matrix), parametrized by a fidelity $f < 1$. However both the ideal **scrambled state** $\hat{U}_S |\mathbf{s}\rangle$ and the fully-mixed state $\hat{I}/2^L$ accurately reproduce the infinite-temperature expectation value. Thus decoherence during the random state preparation process may in fact be helpful, rather than harmful (as long as the circuit \hat{U}_S is temporally random, so as to avoid any nontrivial steady states). This is confirmed by the results of exact density matrix simulations of $L = 12$ qubits in the presence of depolarizing noise, in Fig. 9b. The variance between bit-string states falls exponentially in K (depth of \hat{U}_S) even below the ideal quantum typicality limit of Eq. (21). The subsequent decay is purely due to decoherence: the scrambled state $\Phi_S(\hat{\rho})$ asymptotically approaches the fully mixed state $\hat{I}/2^L$ as the noisy circuit is made deeper.

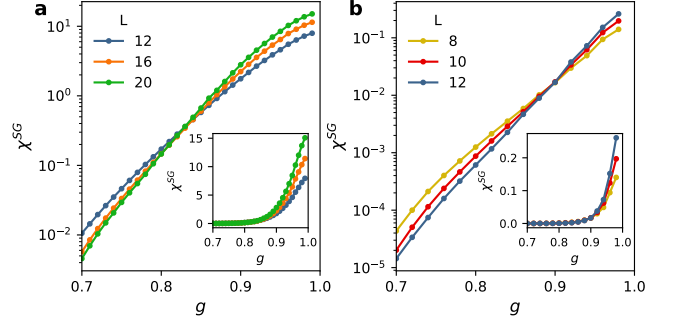


FIG. 10. **Numerical simulations of spin glass order parameter.** **a**, Ideal (noiseless) dynamics. χ^{SG} averaged over even times between $t = 50$ and $t = 60$, over initial bit-string states and over realizations of disorder. At least 4000 realizations are averaged at sizes $L = 12$ and 16 , at least 300 at $L = 20$. Inset: same data on a linear scale. **b**, Noisy dynamics (exact density matrix simulations). Noise is modeled by single-qubit depolarizing channels with Pauli error rate $p = 0.5\%$ after each 2-qubit gate. χ^{SG} is averaged over even times between $t = 50$ and $t = 60$, over initial bit-string states, and over realizations of disorder. At least 1000 realizations are used at sizes $L = 8$ and 10 , at least 100 at $L = 12$. Inset: same data on a linear scale.

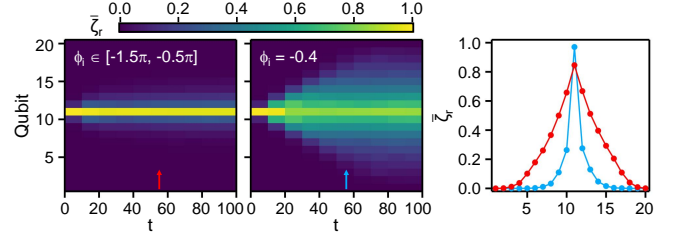


FIG. 11. **Numerical simulations of correlation measurements.** Noiseless simulation of the experiment in Fig. 3d of the main text. Here we simulate the fractional change in $\langle \hat{Z}(t) \rangle$, $\bar{\chi}_r$ (see definition in main text), due to a single bit-flip at Q_{11} in initial condition. The simulation is averaged over 1000 disorder instances for both $\phi_i \in [-1.5\pi, -0.5\pi]$ and $\phi_i = -0.4$.

VI. NUMERICAL RESULTS ON SPIN GLASS ORDER PARAMETER

Here we show results of numerical simulations of the spin glass order parameter used to perform a finite-size analysis of the phases in the main text. We define the order parameter as

$$\chi^{SG} = \frac{1}{L-2} \sum'_{i \neq j} \langle \hat{Z}_i \hat{Z}_j \rangle^2 \quad (27)$$

where the primed sum excludes the edges (qubits Q_1 and Q_L) in order to remove the effects of edge modes from bulk physics. In a phase with glassy order all the expectation values $\langle \hat{Z}_i \hat{Z}_j \rangle$ are finite and χ^{SG} is extensive ($\sim L$). Otherwise, all expectation values asymptotically

vanish and $\chi^{SG}/L \rightarrow 0$.

In Fig. 10a we show results of numerical simulations of χ^{SG} in the absence of noise, at times t between 50 and 60 cycles, as the length of the qubit chain is scaled from $L = 12$ to $L = 20$. A finite-size crossing is visible near $g \simeq 0.83$, separating a side of parameter space (at larger g) where χ^{SG} grows with L , indicative of the MBL-DTC phase, from one (at smaller g) where χ^{SG} decreases with L , indicative of a thermalizing phase. We also note that the finite-size crossing in these data slowly drifts towards higher g as t increases (not shown), as expected from slow thermalization on the ergodic side near the transition.

Repeating the same analysis in the presence of noise yields the data in Fig. 10b. We model noise as a single-qubit depolarizing channel with Pauli error rate $p = 0.5\%$ acting on both qubits after each 2-qubit gate. Simulations are carried out by exact evolution of the density matrix, which is memory-intensive and limits the available system sizes to $L \leq 12$ within reasonable computational resources. (We use this method rather than quantum trajectories⁵¹ because the latter method is impractical for this calculation: as χ^{SG} is a nonlinear function of the state, each expectation $\langle \hat{Z}_i \hat{Z}_j \rangle$ must be averaged over trajectories separately for each disorder realization). We still find a finite-size crossing, though at a considerably higher value of $g \simeq 0.90$. We note that the noisy simulations in Fig. 10b do not include the effects of read-out error and that the depolarizing noise model is not guar-

anteed to be a quantitatively accurate approximation in these structured circuits. Even so, the experimental estimate of the phase transition point $0.84 \lesssim g_c \lesssim 0.88$ is reasonably close to the numerical ones, $g_c \simeq 0.83$ (without noise) and $g_c \simeq 0.90$ (with noise).

VII. NUMERICAL RESULTS OF CORRELATION MEASUREMENTS

The noiseless simulation of the experiment in Fig. 3d of the main text is shown in Fig. 11. Here we generate a total of 1000 disorder instances for both $\phi_i \in [-1.5\pi, -0.5\pi]$ and $\phi_i = -0.4$. The values of $\langle \hat{Z}(t) \rangle$ are simulated with the two initial conditions $|00000000000000000000\rangle$ (ζ_1) and $|00000000001000000000\rangle$ (ζ_2), and the ratio $\bar{\zeta}_r$ is computed using the same method as the main text.

It is seen that the ratio $\bar{\zeta}_r$ from the noise simulation is quite similar to the experimentally measured values, despite no active error-mitigation for this particular quantity. This is likely attributed to the fact that decoherence introduces a damping factor that is approximately the same for both the nominator ($|\zeta_1 - \zeta_2|$) and denominator ($|\zeta_1| + |\zeta_2|$) used to compute $\bar{\zeta}_r$. Consequently, their effects are canceled out after dividing the two quantities.